Journal of Alloys and Compounds 967 (2023) 171845

Contents lists available at ScienceDirect

Journal of Alloys and Compounds

journal homepage: www.elsevier.com/locate/jalcom

Synthesis of nickel cobalt sulfide on Ni foam for improved electrochemical energy storage: Effect of binder-free reverse pulse potentiostatic electrodeposition and redox additive

N.C. Maile [a,b], S.K. Shinde [c], D.–Y. Kim [d], K.C. Devarayapalli [a], Dae Sung Lee [a,*]

[a] Department of Environmental Engineering, Kyungpook National University, 80 Daehak-ro, Buk-gu, Daegu 41566, the Republic of Korea
[b] Department of Chemistry and Chemistry Institute for Functional Materials, Pusan National University, Busan 46241, the Republic of Korea
[c] Department of Physics, Arts, Science and Commerce College, Indapur, Pune 413106, India
[d] Department of Biological and Environmental Science, College of Life Science and Biotechnology, Dongguk University, 32 Dongguk-ro, Biomedical Campus, Ilsandong-gu, Siksa-dong, 10326 Goyang-si, Gyeonggi-do, the Republic of Korea

ARTICLE INFO

Keywords:
Reverse pulse electrodeposition
Nickel cobalt sulfide
Hybrid supercapacitor
Redox additive
Electrodeposition

ABSTRACT

Nickel cobalt sulfide (Ni-Co-S) was grown on 3D conductive Ni foam (NF) using binder-free electrochemical deposition to serve as a positive electrode (NCS@NF) for electrochemical energy storage application. Multiple cycles of reverse pulse potentiostatic electrochemical deposition (RPP-ED) were systematically applied to study their influence on the physico-chemical properties of NCS@NF. During the 300 optimized RPP-ED cycles uniform mesoporous interconnected nanoflakes of Ni-Co-S were formed on NF. The NCS@NF electrode demonstrated remarkable electrochemical storage performance, achieving a maximum areal capacity of 0.590 C cm^{-2} (590 C g^{-1}) in 2 M KOH electrolyte. This remarkable property of NCS@NF can be associated with the improved ionic diffusion at the interconnected nanoflake structure and improved redox transitions at the active sites of nanoflakes. Moreover, the addition of $K_4(CN)_6$ as a redox additive improved the areal capacity of NCS@NF to 2.56 C cm^{-2} (2560 C g^{-1}). Furthermore, an aqueous hybrid supercapacitor was assembled by integrating activated carbon on NF as the negative electrode, while employing NCS@NF as the positive electrode. The aqueous hybrid supercapacitor exhibited an enhanced charge-discharge potential of 1.5 V and demonstrated remarkable stability, maintaining 89% of its performance over 10,000 cycles. Notably, it achieved maximum energy and power densities, 33 μWh cm^{-2} and 6019 μW cm^{-2}, respectively. These results establish its suitability for hybrid supercapacitor applications.

1. Introduction

The increased demand for portable electronics, hybrid-electric transportation vehicles, and energy-harvesting technologies toward sun and wind has emphasized the need for effective energy storage systems [1,2]. Thus, supercapacitor (SC) has received widespread attention as a promising energy storage system because of their high power density and long operational lifespan compared with battery. However, the high manufacturing cost and low energy density limit its commercial applications [2]. Various materials have been explored for SC applications. Among these, carbon-based materials, which exhibit surface-dominant electrochemical double-layer storage, have low electric charge storage. Transition metal oxides and hydroxides have poor conductivity, thereby reducing their charge storage efficiency. In addition, conducting polymers are prone to instability, which hinders their commercial use. The development of advanced electrode materials for SC application could be a solution to these problems [3]. Among different materials, nanoscale transition metal sulfides (TMS) such as $NiCo_2S_4$, $CoNi_2S_4$, and Ni-Co-S have been highly regarded as advanced electrode materials for hybrid SC application because of their remarkable redox activity and good conductivity [4–8]. Different studies have reported the synthesis of TMS for SC electrode using a hydrothermal method [9,10], chemical bath deposition [7], co-precipitation [11], electrochemical deposition [4,12], and a solvothermal method [13]. Among these methods, a binder-free electrodeposition method can produce highly uniform and porous active material surfaces for SC electrodes, which can promote electrochemical activity and show enhanced charge storage capacity during the electrochemical reaction

* Corresponding author.
E-mail address: daesung@knu.ac.kr (D.S. Lee).

https://doi.org/10.1016/j.jallcom.2023.171845
Received 7 July 2023; Received in revised form 18 August 2023; Accepted 21 August 2023
Available online 22 August 2023

[4,5,12,14,15]. Moreover, the crystallinity, thickness, and morphology of the electro-synthesized material can be easily controlled by various electrodeposition parameters [15,16].

The reverse pulse potentiostatic electrochemical deposition (RPP-ED) is a simple, time-saving technique that have been used for producing highly pure materials for various applications in electrochemistry. By adjusting the deposition conditions, this method may regulate the grain size of nanostructures and hardness of the produced material [17]. In RPP-ED, short pulses of reverse potentials are applied to the conducting surface, resulting in successive oxidative and reductive reactions. This technique can prevent the underpotential deposition of unwanted materials, and short pulse prevents the bulk growth of the materials [18]. Previous studies have used RPP-ED for the synthesis of active materials for different applications, such as hydrogen evolution reaction (HER)/oxygen evolution reaction (OER)[19], dye-sensitized solar cells [20], and SCs [20,21]. Kim et al. prepared NiP material on a Cu foil for HER and OER applications [19]. Krishnan et al. prepared dendritic nanostructures of $NiCo_2S_4$ on FTO for efficient counter electrodes for dye-sensitized solar cells. In particular, Chou et al. prepared Ni_3S_2 nanoflakes on Ni foam (NF), which showed 179.5 mAh g^{-1} [20]. Dhaiveegan et al. prepared Ni_3S_2 on a flexible carbon fiber cloth, which showed 600 F g^{-1} [21]. Chou et al. prepared a Ni_aCo_bS nanosheet on NF, which showed 1.75 F cm^{-2} at 5 mV s^{-1} [5]. Ni-Co-S-based active materials can be further developed by RPP-ED, which could facilitate stable redox reactions on the material surface. Furthermore, many researchers have attempted to generate redox reactions within the electrolyte to boost the overall performance of SCs. In achieving this, redox additives such as $K_4[Fe(CN)_6]$ have been added to the electrolytes [22,23]. Redox transitions on the active material are limited; thus, the addition of redox-active additives can enhance the overall performance of SC [23].

Here, mesoporous interconnected nanoflakes of Ni-Co-S were grown on Ni foam (NCS@NF) as a positive electrode for hybrid SC application using simple RPP-ED. The NCS@NF electrode was prepared for a varying number of pulse cycles, and the highest electrochemical performance was obtained for 300 pulse cycles. Furthermore, the charge storage performance of the electrode was improved by adding redox additives such as $K_4[Fe(CN)_6]$. The useful and practical aspects of the NCS@NF electrode were explored by assembling aqueous hybrid SC.

2. Materials and methods

2.1. Material preparation for NCS@NF

In preparing the NCS@NF electrode, NF was used as 3D porous framework substrate for growing Ni-Co-S nanostructures. Prior to synthesis, NF was successively cleaned by ultrasonication in diluted HCL, ethanol, and deionized (DI) water. The electrolyte was prepared using 5 mM $Ni(NO_3)_2$, 10 mM $Co(NO_3)_2$, and 0.1 M thiourea in DI water at room temperature. The 1200 Premium workstation (WizMAC, Republic of Korea) was used for RPP-ED in three-electrode mode, where the cleaned NF, platinum plate, and saturated calomel electrode (SCE) served as the working electrode, counter electrode, and reference electrode, respectively. The RPP-ED synthesis of Ni-Co-S was conducted by applying continuous cycles of potentiostatic pulse to NF, with an anodic bias of 0.6 V for 4 s and a cathodic bias of − 1.7 V for 2 s. Different NCS@NF electrodes were prepared for 100, 200, 300, and 400 RPP-ED cycles, labeled as A1, A2, A3, and A4, respectively. Mass loading for A1, A2, A3, and A4 was measured as ~0.8, 0.9, 1.0, and 1.1 mg cm^{-2}, respectively. After preparation, all electrodes were tested for their physical and electrochemical properties.

2.2. Assembling aqueous hybrid SC device

The negative electrode for aqueous hybrid SC was prepared using an appropriate amount of activated carbon as an active material, which was drop-casted onto the NF (AC@NF) [24]. The prepared A3 was used as positive electrode. Both electrodes were dipped into an electrolyte solution containing 2 M KOH and 0.1 M $K_4[Fe(CN)_6]$ to form an aqueous hybrid SC device assembly, which was then tested for their electrochemical properties.

2.3. Material characterization

The surface morphology and microstructure of A1, A2, A3, and A4 were investigated by field-emission scanning electron microscopy (FE-SEM; HITACHI SU8230 [Japan]). X-ray diffraction (XRD) spectra carried out using a Panalytical X-ray diffractometer (EMPYREAN, UK) with Cu K_α radiation of $\lambda = 1.54$ Å. A Raman spectrometer (Renishaw inViareflex spectrometer, Gloucestershire, UK) was used for Raman experiments. Elemental distribution in the samples was analyzed using energy-dispersive spectroscopy (EDS; Oxford Ultim Max100, UK) and X-ray photoelectron spectroscopy (XPS; ThermoFisher-NEXSA, USA).

2.4. Electrochemical measurement

The electrochemical properties of A1, A2, A3, and A4 were tested in half-cell configuration using the WizEIS 1200 Premium workstation (WizMAC, Republic of Korea). For this purpose, the NCS@NF was tested as a working electrode without any further fabrication, while a platinum plate and Hg/HgO were used as the counter and reference electrode, respectively. Electrochemical impedance spectroscopy (EIS) was performed using the Ivium CompactStat.h instrument. The assembled hybrid SC was also tested using similar instruments.

3. Results and discussion

3.1. Formation mechanism of Ni-Co-S on NF

In understanding the growth of the material, the CV of cleaned NF was performed in the electrolyte consisting of $Ni(NO_3)_2$, $Co(NO_3)_2$, and thiourea (Fig. 1a). During a negative bias scan from 0.5 to − 1.0 V, the drastic decrease of current is followed by a steady plateau from − 0.1 to − 0.34 V, which can be associated with the codeposition of Ni- and Co-forming monolayers [15]. The electroreduction of nitrate ions initiates the production of -OH^-, and thiourea is reduced in the presence of -OH^- to generate S^{2-}. Consequently, the co-precipitation of Ni-Co-S occurs on the surface of NF. This phenomenon can be characterized by the decrease of j from − 0.34 to − 2 V with a broad reduction peak at − 0.75 V [6,16]. Furthermore, a negative bias $E < -1.0$ V leads to the additional reduction of water and the production of more -OH^-, resulting in increased cathodic current and further reduction of thiourea, thereby promoting Ni-Co-S precipitation [16]. Chemical routes involved in the deposition can be described as follows [6,15,16,25]:

$$NO_3^- + H_2O + 2e^- \rightarrow NO_2^- + 2OH^- \quad (1)$$

$$NO_2^- + 6H_2O + 6e^- \rightarrow NH_4^+ + 8OH^- \quad (2)$$

$$2H_2O + 2e^- \rightarrow 2OH^- + H_2 \quad (3)$$

$$SC(NH_2)_2 + 2OH^- \rightarrow S^{2-} + OC(NH_2)_2 + H_2O \quad (4)$$

$$M^{2+} + S^{2-} \rightarrow MS;\ (M{=}Co,\ Ni) \quad (5)$$

During the positive bias scan, a broad anodic peak centered around 0.12 V was observed, which can be attributed to the oxidation of unreacted Co and Ni species, as well as thiourea oxidation [16,26].

Underpotential reduction deposition ($E_{red} > -0.34$ V) can reduce metal species on NF, which could be avoided at a bias of $E_{red} < -0.34$ V. However, thiourea reduction in aqueous media at a steady lower bias of $E_{red} < -1.0$ V could continuously generate hydrogen bubbles on the NF surface, thereby hindering the continuous electrodeposition of Ni-Co-S. This issue might be addressed by applying a short reduction pulse of lower bias E_{red} [15,16]. Given this advantage, several authors have

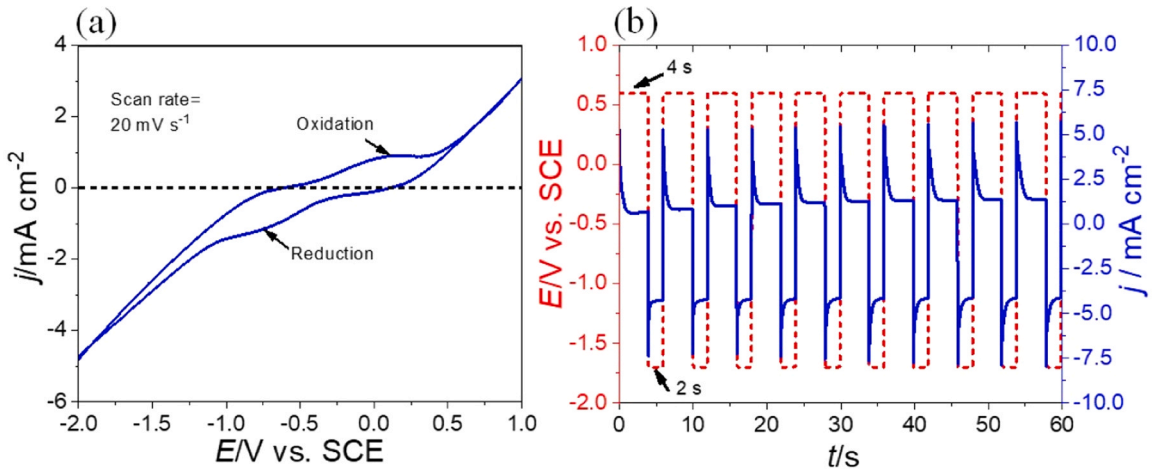

Fig. 1. (a) CV of NF in the electrolyte consisting of 5 mM $Ni(NO_3)_2$, 10 mM $Co(NO_3)_2$, and 0.1 M thiourea recorded at a υ of 20 mV s^{-1}, and (b) Collective plot of *E vs. t* and *j vs. t* for the first 10 consecutive RPP-ED cycles.

reported the electrodeposition of materials using a short reduction pulse of lower bias E_{red}. Anuratha et al. used the bias pulse of $E_{red} = -1.2$ V *versus* SCE for the codeposition of $NiCo_2S_4$ on the FTO surface [16]. Chou et al. used $E_{red} = -1.24$ V *versus* Ag/AgCl for Ni_aCo_bS nanosheet on NF [5]. Similarly, Chassaing et al. used $E_{red} = -2.0$ to -3.0 V *versus* SCE for the codeposition of Ni-Mo alloys [27]. Shinde et al. reported the electrodeposition of Fe_2O_3 on FTO using two electrode systems and used reduction bias pulse of $E_{red} = -6$ V *versus* platinum [17]. Based on the abovementioned reports, a reduction bias pulse has been followed by an oxidation bias pulse (E_{ox}), which is necessary to oxidize loosely bound species that are created during the E_{red} step. The CV (Fig. 1a) highlights complete oxidation at the NF surface at $E_{ox} > 0.6$ V.

Here, for NCS@NF, a E_{red} of -1.7 V was applied to NF for 2 s for Ni-Co-S deposition, and a E_{ox} of 0.6 V was applied for 4 s to NF for the removal of unreacted species, completing one RPP-ED cycle. This method ensures the growth of Ni-Co-S on NF [Fig. S1]. In this way, NCS@NF was synthesized at different RPP-ED cycles to obtain the optimal electrochemical performance for SC electrode application. The plot of observed *j* for the first 10 consecutive RPP-ED cycles is shown in Fig. 1(b). Under the influence of $E_{red} = -1.7$ V, the initial sharp decrease in *j* may indicate a large amount of electroreduction at the working electrode, which changes the precursor concentration. This phenomenon is followed by the 3D growth of Ni-Co-S, as indicated by the gradual increase and stabilization of *j* over time [28,29]. However, when applying a reverse bias of $E_{ox} = 0.6$ V, the sharp increase in *j* highlights the oxidation of a large amount of unreacted species followed by the gradual decrease and stabilization of *j* over time, indicating steady oxidation reactions, which might be attributed to the continuous dissolution of Ni-Co-S in the presence of excess thiourea [16,26].

3.2. Phase composition and morphological characterization of NCS@NF

Fig. 2 shows the surface morphology of A1, A2, A3, and A4. All samples exhibit random distribution of flakes with different porous morphologies. At E_{red}, the bulk reduction of thiourea and water generates nucleation sites all over the NF surface. The applied short duration of E_{red} avoids mass transfer at the nucleation sites for the growth of material. Using each E_{ox} pulse, loosely bound species can be oxidized. Consequently, in each repetitive RPP-ED cycle, the 3D bulk growth is avoided, and nucleation sites grow slowly to form a randomly oriented flake structure all over the surface [5,30,31]. For 100 (Fig. 2 [a, b]) and 200 (Fig. 2 [c, d]) RPP-ED cycles, the uniform growth of nanoflakes with random distribution is observed in A1 and A2, respectively. Pores in A2 are more visible compared with those in A1. This growth continued for 300 RPP-ED cycles (Fig. 2 [e, f]). Compared with A2, A3 shows a higher density of flakes and void pores. Further growth is observed for 400 RPP-ED cycles (Fig. 2f). For A4, the agglomeration of nanoflakes forms bulk centers, which are distributed randomly on the surface (Fig. 2g). A close view (Fig. 2h) shows that these bulk centers consist of interconnected thick flakes covering. This overgrowth causes distinct cracks on the A4 surface (Fig. 2g). Surface analysis shows that A2 and A3 have firm growth and uniform porous structure, which can promote the easy diffusion of electrolyte ions [24].

Sharp XRD peaks observed at 2θ of 44.59°, 51.84°, and 76.37° in A1, A2, A3, and A4 (Fig. 3a) result from conducting NF [24]. Samples do not show any other peaks, indicating poor crystallinity in NCS@NF. Previously, Li et al. reported room temperature synthesis of amorphous nickel cobalt sulfide nanoparticles [11]. For confirmation, the Raman spectrum of A3 were recorded (Fig. 3b). The spectrum showed different scattering peaks for different Raman active modes, which are similar to those observed for $NiCo_2S_4$ [32,33]. The stretching and bending of S-Ni_{tera}-S can be represented by $A_{1\,g}$(385 cm^{-1}) and E_g(238 cm^{-1}) modes. Other peaks such as 150, 305, and 347 cm^{-1} can be three $T_{2\,g}$ modes of asymmetric bending of S-Ni_{tera}-S [33]. The peak observed at 527 cm^{-2} can be associated with the $T_{2\,g}$ mode, as laser heating can easily oxidize metal sulfides [32–34].

Furthermore, XPS analysis of A3 was performed. The XPS core level spectrum (Fig. 3c) shows distinct peaks for S, O, Co, and Ni. The deconvolution of the Ni 2p orbital (Fig. 3[d]) indicates the presence of 2^+ and 3^+ oxidation states of Ni. The peak observed at 874.9 eV in 2 $p_{1/2}$ and 857.6 eV in 2 $P_{3/2}$ can be associated with Ni^{3+}; however, the peak observed at 873.2 eV in 2 $p_{1/2}$ and 855.8 eV in 2 $P_{3/2}$ can be associated with Ni^{2+} [35,36]. Similarly, the deconvolution of the Co 2p orbital indicates the presence of 2^+ and 3^+ oxidation states of Co. The peak observed at 798.2 eV at 2 $p_{1/2}$ and 783.6 eV at 2 $p_{3/2}$ can be associated with Co^{2+}; however, the peak observed at 796.7 at 2 $p_{1/2}$ and 781.3 eV at 2 $p_{3/2}$ can be associated with Co^{3+} [20,35]. The deconvolution of the S 2p orbital shows peaks at 163.3 and 161.8 eV, which can be associated with 2 $p_{1/2}$ and 2 $p_{3/2}$ orbital highlighting the presence of S^{2-} [20]. The peak at 169.8 eV is due to adsorbed oxygen leading to SO_4^{2-} [37]. The deconvolution of the O 1 s orbital shows the presence of peaks at 533.0 and 531.4 eV, which is mostly associated with O from adsorbed water and low coordinated defect sites. The results from Raman scattering and XPS indicate that hydrous Ni-Co-S was formed on NF with abundant active sites consisting of Ni^{2+}, Co^{2+}, Ni^{3+}, and Co^{3+} can be confirmed by SEM [20,24,38]. The EDS spectrum of A3 was recorded to study the distribution of elements. Similar to XPS, EDS showed (Fig. 3[h]) the presence of S, O, Co, and Ni. An increased atomic percentage of Ni and O elements can be attributed to the creation of a hygroscopic thin film of Ni-Co-S on the surface of the NF [16]. Furthermore, elemental mapping

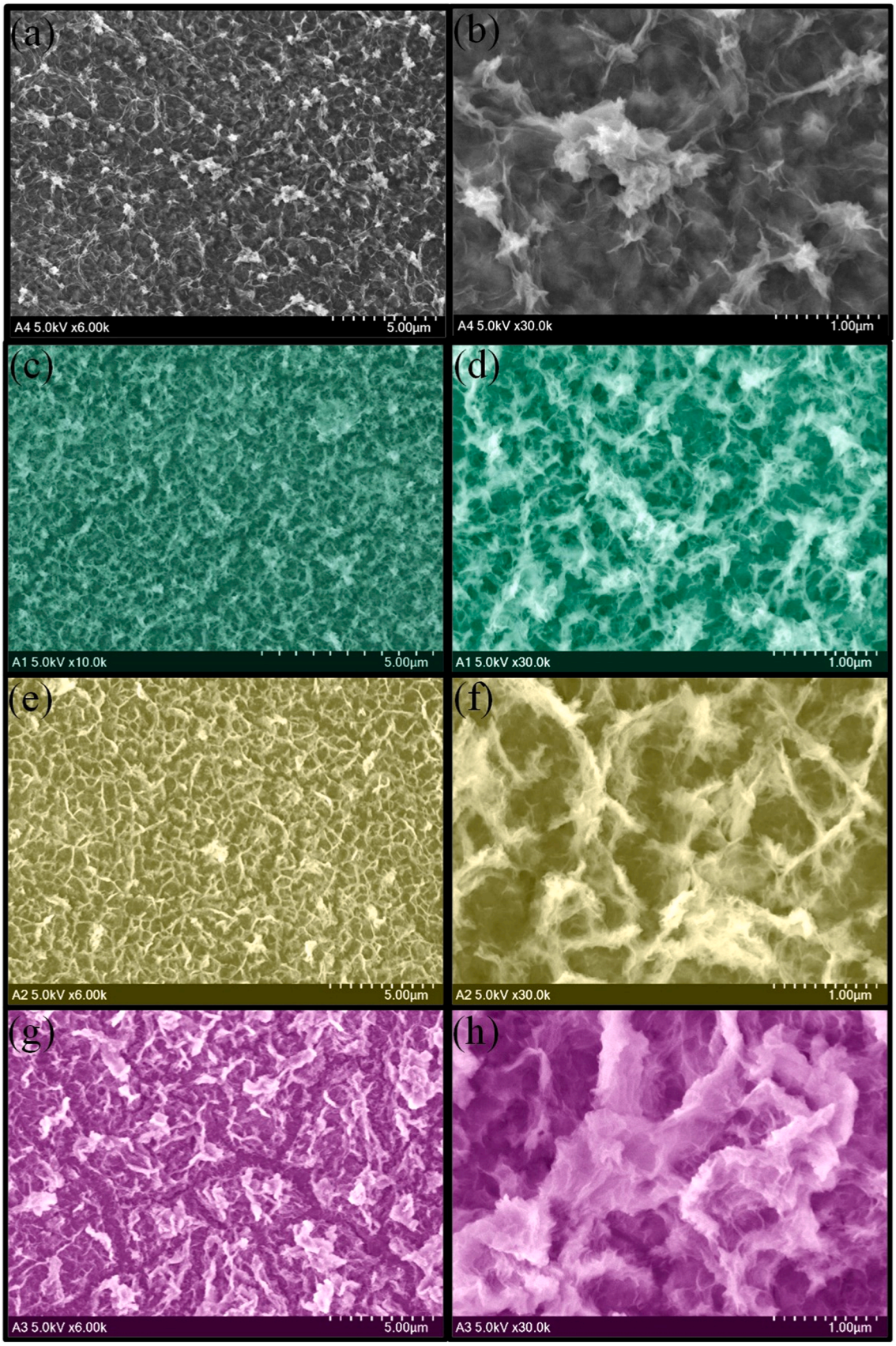

Fig. 2. FE-SEM image of A1 (a–b), A2 (c–d), A3 (e–f), and A4 (g–h).

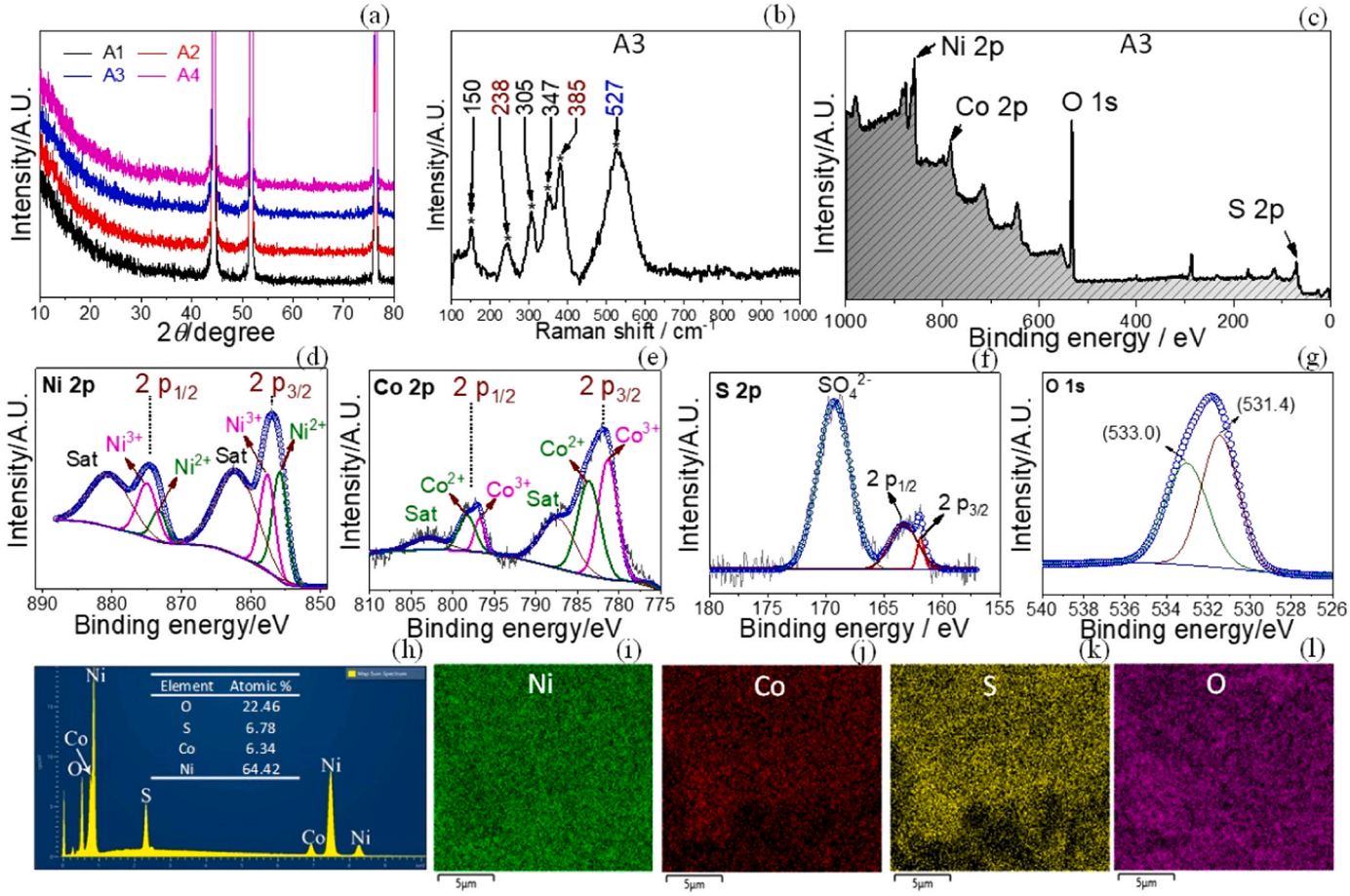

Fig. 3. (a) XRD patterns of A1, A2, A3, and A4, (b) Raman spectrum of A3, and (c) XPS survey spectrum of A3. Deconvoluted high-resolution XPS curves for Ni 2p(d), Co 2p(e), S 2p(f), and O 1 s(g) orbitals, and (h) EDS spectrum of A3 (inset: element atomic %). Elemental mapping images of A3 for Ni(i), Co(j), S(k), and O(l).

images (Fig. 3 [i–l]) show a uniform distribution of elements.

3.3. Electrochemical performance of NCS@NF

3.3.1. CV performance

First, the electrochemical performance of the prepared NCS@NF was tested in 2 M KOH. The obtained CV plots of A1, A2, A3, and A4 performed at a scan rate (ν) of 20 mV s^{-1} are shown in Fig. 4a. All CV profiles show a broad oxidation and reduction peak in the E range from − 0.1–0.6 V, indicating the presence of reversible redox electrochemical reactions at the electrode [9,34]. The area under the CV curve highlights the electrochemical charge storage performance of NCS@NF. With the increase of RPP-ED cycles from 100 to 400 (Fig. 4a), the area under CV and peak intensity increased up to 300 RPP-ED cycles and thereafter decreased for 400 RPP-ED cycles. Based on FE-SEM, the growth of porous nanoflakes with an increased mass loading of NCS@NF with each RPP-ED cycle developed abundant active sites for faradaic transitions, resulting in increased performance. However, overgrowth at 400 RPP-ED cycles might introduce bulk resistance to the electrode. The FE-SEM image of A4 shows that the voids are covered with overgrown nanoflakes, which could effectively reduce active sites and restricts electrolyte ionic diffusion at NCS@NF, thereby reducing its performance. Fig. 4b shows the CV curves of A3 obtained for different ν. All the CV curves show broad oxidation and reduction peaks, which result from cumulated redox reactions at NCS@NF [9,34]. Moreover, as ν increases, the oxidation and reduction peak of CV shift toward high and low ends of E, respectively. This electrode polarization is due to the change in internal resistance under the influence of applied ν [38,39]. During CV, the stored and retrieved current (j) under the influence of ν at given E can be divided into two components, namely, surface-induced current ($j_{surf} \propto \nu$) and diffusion-induced current ($j_{diff} \propto \nu^{1/2}$), as given by $j^{\nu}(E) = j^{\nu}_{surf}(E) + j^{\nu}_{diff}(E)$ [15,38]. Here, the j_{surf} component represents kinetically faster reactions, which consist of non-faradic reactions *via* electrostatic adsorption and faster reversible faradic reactions occurring at the electrode surface caused by the easy access of active sites for electrochemical interactions. Meanwhile, the j_{diff} component is due to the diffusion of electrolyte ions toward active sites present at voids and nanoflakes, followed by faradic reactions at these active sites. Linear fitting between j_{peak} and $\sqrt{\nu}$ (inset of Fig. 4b) highlights that most charge storage occurring at active sites of NCS@NF nanoflakes is due to the diffusion and subsequent faradic interaction of electrolyte ions. The plot of CV associated with $j^{\nu}(E)$ and $j^{\nu}_{surf}(E)$ at $\nu = 20$ mV s^{-1} (Fig. 4c) shows that most of the surface currents are generated at all regions of CV, except for the extensive oxidation and reduction peak area where diffusion reactions predominantly govern the processes. Evidently, the contribution of J_{surf} also varies with ν. The contribution of J_{surf} in CV increases with the increase of ν (inset of Fig. 4c) [40]. Low ν essentially provides enough time for settling and diffusion of electrolyte ions at Ni-Co-S nanoflakes. This is essential for diffusion-based faradic transitions. With increasing ν, ions do not get enough time to settle; thus, active sites from the surface participate more in charge storage [15]. The CV of A1, A2, and A4 at different ν also show similar charge–discharge behavior (Fig. S2[a–c]). The areal capacity (Q_{cv}) of individual NCS@NF was estimated by analyzing the CV curves. The value of Q_{cv} was estimated by using the following relation [41]:

$$Q_{cv} = (\int IdE)/(2\times\nu\times A)\ldots(\text{C cm}^{-2}) \quad (6)$$

where $\int IdE$ is the integral area under the CV, and A is the geometrical

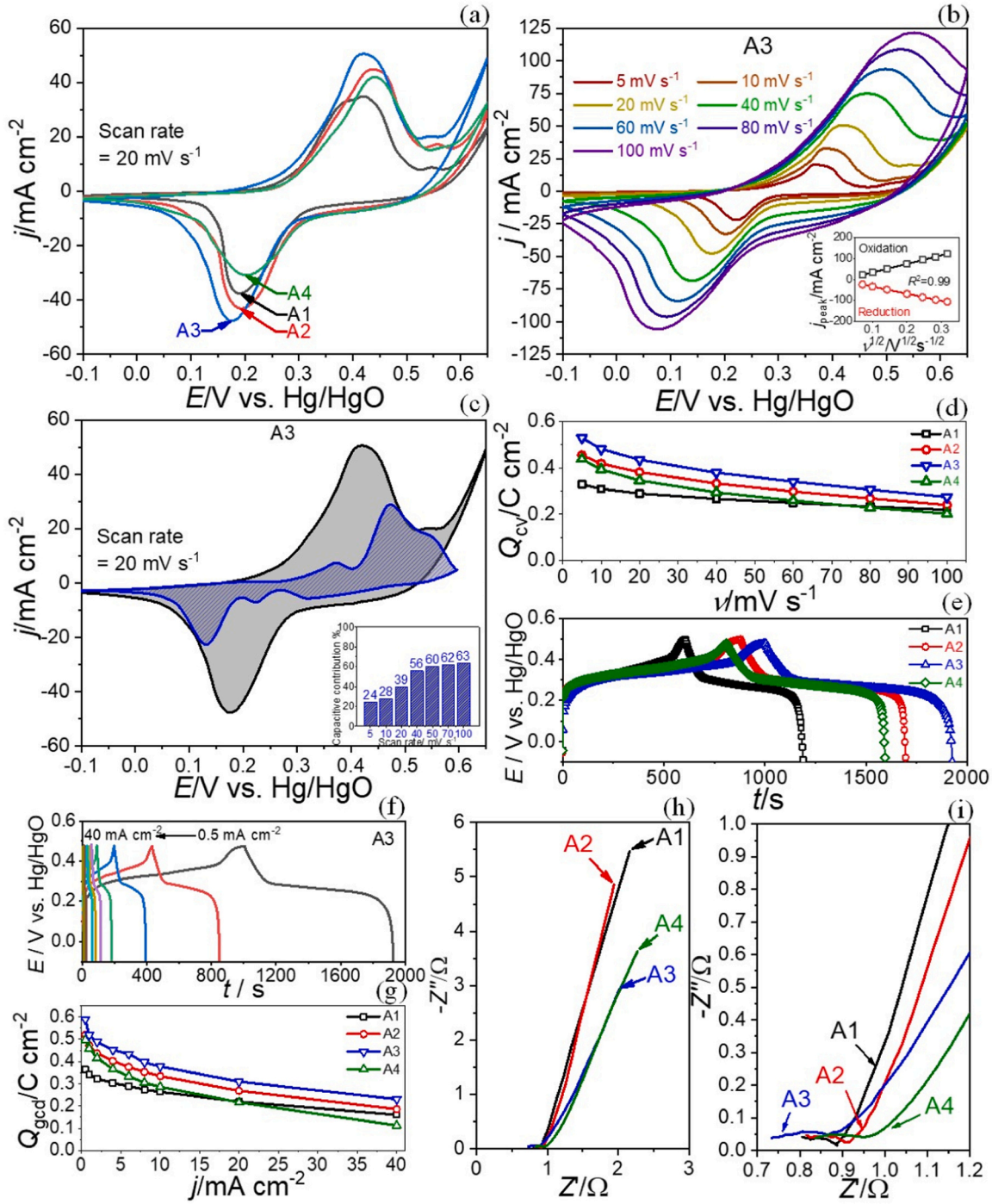

Fig. 4. (a) CV curves of A1, A2, A3, and A4 recorded at $\nu = 20$ mV s^{-1}, (b) CV curves of A3 at different ν [inset: plot of j_{peak} *vs.* $\upsilon^{1/2}$], (c) Plots of recorded CV curve and CV curve associated with capacitive contribution in A3, (d) Plots of estimated Q_{cv} at different ν for A1, A2, A3, and A4, (e) GCD curves of A1, A2, A3, and A4 recorded at $j = 0.5$ mA cm^{-2}, (f) GCD curves of A3 at different j, (g) Plots of estimated Q_{gcd} at different j for A1, A2, A3, and A4, (h) Nyquist plots of A1, A2, A3, and A4, and (i) High-frequency region of Nyquist plots of A1, A2, A3, and A4.

surface area of NCS@NF under testing. The plot of Q_{cv} *vs.* ν (Fig. 4[d]) clearly illustrates that A3 exhibits the highest capacity across all ν values. It exhibited a maximum of 0.53 C cm^{-1} (530 C g^{-1}) at $\nu = 5$ mV s^{-1}. Overgrowth in A4 might reduce the electronic conductivity of NCS@NF and ionic diffusion pathways at active sites, resulting in a comparatively lower areal capacity rate performance.

3.3.2. GCD and EIS performance

All electrodes were subjected to GCD at different values of j from 0.5 to 40 mA cm^{-2}. The *E-t* curve obtained for A1, A2 A3, and A4 at $j = 0.5$ mA cm^{-2} (Fig. 4e) showed battery-like nonlinear charging–discharging behavior of NCS@NF in 2 M KOH. This typical process involves an initial enhancement in potential caused by fast surface charging at the electrode, followed by a potential plateau caused by slow diffusion-controlled faradaic charging, with similar discharging behavior [15,24]. Symmetry across charging and discharging GCD profiles indicates the good electrochemical reversibility of NCS@NF [15, 42]. A remarkable performance of NCS@NF prepared for 300 RPP-ED cycles is shown by A3, which reaches the maximum charge–discharge time. At different j values, the electrochemical reversibility performance

of A3 is retained (Fig. 4f). Similarly, A1, A2, and A4 also exhibited similar charge–discharge behavior (Fig. S2 [d–f]). The areal capacity (Q_{gcd}) of an individual electrode can be estimated by analyzing GCD curves using the following relation [43].

$$Q_{gcd}=(2i\int Edt)/(\Delta E\times A)\ldots(\text{C cm}^{-2}) \quad (7)$$

where i is the discharge current, $\int Edt$ is the integral area under the discharge GCD curve, dt is the discharge time, and ΔE is a potential window. The plot of Q_{gcd} at different j (Fig. 4g) shows that A3 has the maximum capacity compared with A1, A2, and A4 at all j values. Similar to the observed rate performance in Q_{cv} at different ν, A4 shows the lowest areal capacity rate performance in Q_{gcd}. Here, A3 shows a maximum Q_{gcd} of 0.59 C cm^{-2} (590 C g^{-1}/163 mA h g^{-1}) at $j = 0.5$ mA cm^{-2}. This maximum Q_{gcd} of NCS@NF is higher than that of some previously reported Ni- and Co-sulfide-based SC electrodes [10,13, 41,44–49].

In studying the electrochemical properties, EIS analysis was performed on NCS@NF in the frequency range of 10^{-1} to 10^{5} Hz. The Nyquist plots of A1, A2, A3, and A4 are shown in Fig. 4h. All plots exhibit a pseudo-semicircle at the high-frequency region (Fig. 4i) and a straight line at the low-frequency region. The intercept of the curves on

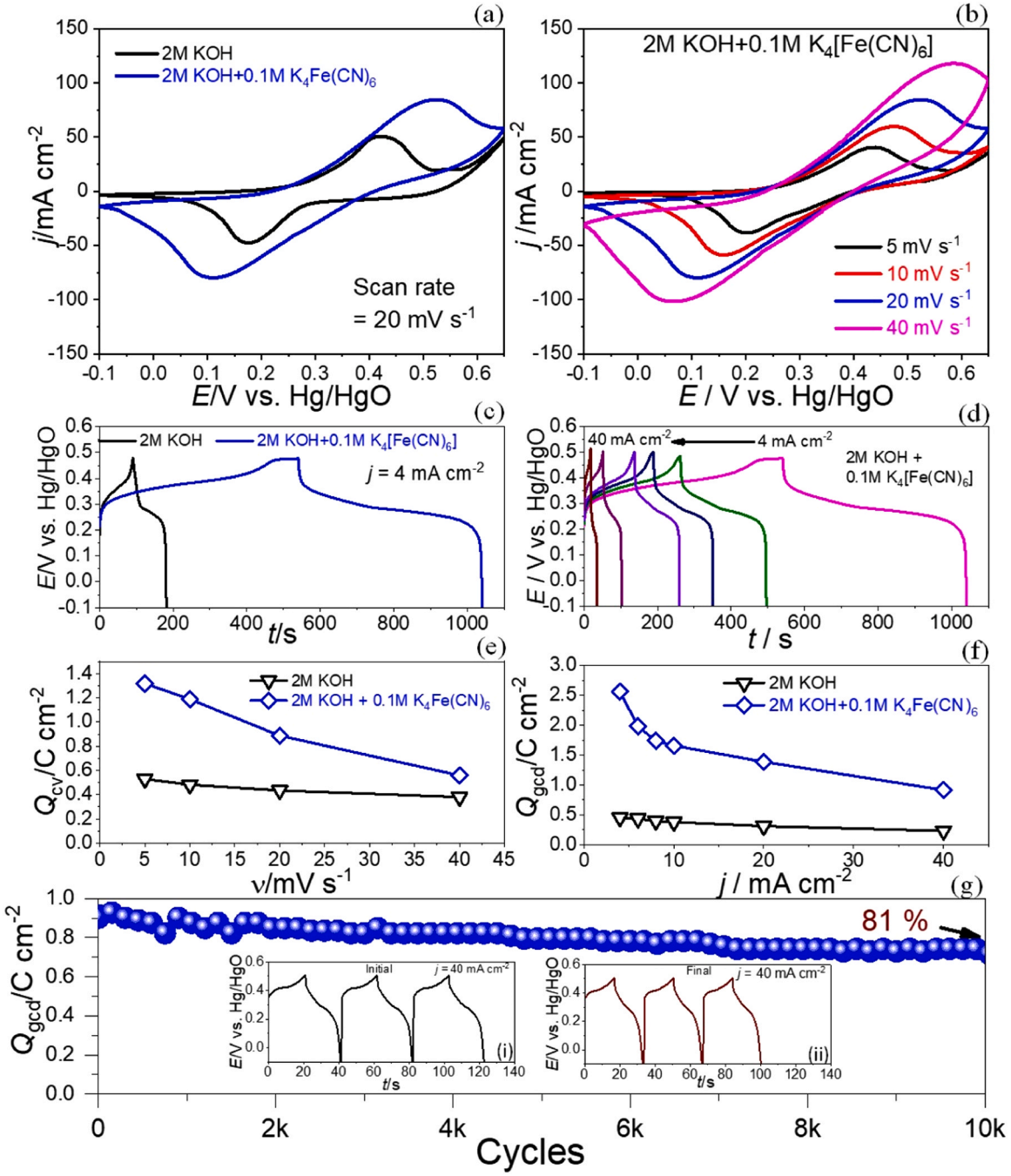

Fig. 5. (a) CV curve of A3 in 2 M KOH and 2 M KOH + 0.1 M $K_4[Fe(CN)_6]$ at 20 mV s^{-1}, (b) CV curve of A3 at different ν in 2 M KOH + 0.1 M $K_4[Fe(CN)_6]$, (c) GCD curves of A3 in 2 M KOH and 2 M KOH + 0.1 M $K_4[Fe(CN)_6]$ at 4 mA cm^{-2}, (d) GCD curves of A3 at different j in 2 M KOH + 0.1 M $K_4[Fe(CN)_6]$, (e) Plot of the estimated Q_{cv} for A3 at different ν in 2 M KOH and 2 M KOH + 0.1 M $K_4[Fe(CN)_6]$, (f) Plots of the estimated Q_{gcd} for A3 at different j in 2 M KOH and 2 M KOH + 0.1 M $K_4[Fe(CN)_6]$, and (g) Plot of the estimated Q_{gcd} for A3 at 40 mA cm^{-2} in 2 M KOH + 0.1 M $K_4[Fe(CN)_6]$ electrolyte for 10,000 successive cycles (inset: the initial[*i*] and final[ii] three consecutive GCD cycles).

the Z′-axis gives the value of the electrical impedance of electrode exhibited during charging and discharging in the electrolyte, which is referred to as solution resistance (R_s) (Fig. S3 [c, g, k, and o]). However, the diameter in the high-frequency region can be observed because of electrolyte ionic diffusion, which is known as diffusion resistance (R_{ct}). The simulation of EIS curves with equivalent circuit (inset of Fig. S3 [a, e, i, and m]) estimated the R_s value of A1, A2, A3, and A4 as 0.71, 0.76, 0.74, and 0.79 Ω, respectively[24,50]. Increasing RPP-ED cycles from 100 to 300, the R_s value of NCS@NF increased except at 300 RPP-ED cycle. This result indicates that more conducting pathways are generated in A3 because of the uniform porous distribution of nanoflakes [15]. Similarly, the R_{ct} value of A1, A2, A3, and A4 is estimated as 0.51, 0.14, 0.11, and 0.16 Ω respectively. The lowest R_{ct} of A3 suggests that short ionic diffusion pathways are developed at Ni-Co-S nanoflakes for effective charge-transfer interactions of electrolyte ions [24]. The Bode plots are also supporting the results (Fig. S3 [d, h,l, and p]).

3.4. Effect of the addition of electroactive species $K_4(Fe(CN)_6)$

The enhancement in the electrochemical storage can be achieved by the addition of a redox additive to the electrolyte [22,51]. During the charge–discharge process, additional electrons can be transferred between the electrode and redox species, thereby improving the overall charge-storage efficiency of the device [22]. In this study, the addition of 0.1 M $K_4(Fe(CN)_6)$ to 2 M KOH significantly enhanced the integrated area of CV curve of A3 recorded at 20 mV s^{-1} (Fig. 5a). The presence of $K_4(Fe(CN)_6)$ provided additional electrons to Ni-Co-S nanoflakes by undergoing redox transformation [22,52].

$$[Fe(II)(CN)_6]^{4-} \leftrightarrow [Fe(III)(CN)_6]^{3-} + e^- \quad (8)$$

At different ν, the CV curves of A3 in the modified electrolyte show a broad oxidation and reduction peak, with peak j increasing with the increase of ν (Fig. 5b). Therefore, the faradic reaction of $K_4(Fe(CN)_6)$ is reversible at NCS@NF. During GCD measurement of A3 at $j = 4$ mA cm^{-2} (Fig. 5c), a significant enhancement in charge–discharge time is observed because of the addition of 0.1 M $K_4[Fe(CN)_6]$ in 2 M KOH. The symmetry across the charge–discharge profile of A3 is consistent at different j in the modified electrolyte (Fig. 5d). Therefore, the diffusion of $[Fe(CN)_6]^{4-/3-}$ at Ni-Co-S nanoflakes is followed by reversible faradic interactions, enabling an additional electron transfer, and these interactions might be non-destructive to NCS@NF. Calculations showed that the increment in Q_{cv} is significantly high in the modified electrolyte at different values of ν ranging from 5 to 40 mV s^{-1} (Fig. 5e). The CV studies estimated the maximum Q_{cv} of 1.31 C cm^{-2} (1310 C g^{-1}) at 5 mV s^{-1} caused by the presence of 0.1 M $K_4[Fe(CN)_6]$, which is significantly higher than the maximum 0.53 C cm^{-2} (530 C g^{-1}) in 2 M KOH at the same ν. Similarly, a significant enhancement in Q_{gcd} was observed at different j values ranging from 4 to 40 mA cm^{-2} in the modified electrolyte (Fig. 5f). The GCD studies estimated the maximum Q_{gcd} of 2.56 C cm^{-2} (2560 C g^{-1}) in the modified electrolyte at $j = 4$ mA cm^{-2}, which is higher than 0.45 F cm^{-2} (450 C g^{-1}) in 2 M KOH at the same j. The stability of A3 in the modified electrolyte was performed by continuous GCD cycling at 40 mA cm^{-2}. The plot of estimated Q_{gcd} at continuous GCD cycles is shown in Fig. 5g. After 10,000 cycles, 81% of the initial Q_{gcd} was sustained, indicating the good cyclic performance of NCS@NF in the modified electrolyte. The inset shows the initial (Fig. 5g[i]) and final (Fig. 5g[ii]) three consecutive GCD cycles. The GCD curves maintained their charge–discharge profile after the cyclic run.

3.5. Electrochemical performance of hybrid SC

Given its enhanced performance in the presence of $K_4[Fe(CN)_6]$ in KOH, a hybrid SC[AC@NF//NCS@NF] was assembled using AC@NF as the negative electrode and A3 as the positive electrode in a modified electrolyte consisting of 0.1 M $K_4[Fe(CN)_6]$ and 2 M KOH. The plots of CVs recorded at $\nu = 40$ mV s^{-1} in the modified electrolyte are shown in Fig. 6a, which demonstrates the electrochemical storage of AC@NF in the potential range of − 1.0 to − 0.1 V *versus* Hg/HgO, as well as A3 in the potential range of − 0.2–0.65 V *versus* Hg/HgO. Based on the CV, the electrochemical storage of AC@NF and NCS@NF resembled with EDLC and battery-like behavior. The resulting CV of AC@NF//NCS@NF was near-rectangular, exhibiting pseudocapacitive behavior at different potential windows (Fig. 6b). Based on the CV, the potential window of 1.5 V is best suited for further electrochemical studies. This near-rectangular pseudocapacitive CV behavior of AC@NF//NCS@NF is sustained at different ν values from 5 to 100 mV s^{-1}, with j increasing with the increase of ν (Fig. 6c). This finding indicates the high reversibility and excellent performance of AC@NF//NCS@NF. In addition, the GCD of AC@NF//NCS@NF was performed at different j ranging from 1 to 10 mA cm^{-2}, showing nearly linear charge–discharge behavior and highlighting pseudocapacitive GCD behavior similar to CV (Fig. 6d). Eqs. 6 and 7 were used to estimate Q from CV and GCD. Given the pseudocapacitive behavior of the SC, the areal capacitance was estimated using the following relation:

$$C_A = Q/\Delta E \left(\text{F cm}^{-2}\right) \quad (9)$$

The areal energy (E_A) and power (P_A) densities can be estimated from C_A [38].

$$E_A = \frac{1}{2}\frac{C_A(\Delta E)^2}{3600}\left(\text{Wh cm}^{-2}\right) \quad (10)$$

$$P_A = \frac{E_A}{\Delta t} \times 3600\left(\text{W cm}^{-2}\right) \quad (11)$$

The maximum estimated Q_{cv} is 165 mC cm^{-1} (C_A=110 mF cm^{-2}) at 5 mV s^{-1}. For 100 mV s^{-1}, Q_{cv} is sustained as 89 mC cm^{-2} (C_A=59 mF cm^{-2}) as shown in Fig. 6(e). The maximum estimated Q_{gcd} from GCD was 158 mC cm^{-1} (C_A=105 mF cm^{-2}) at 1 mA cm^{-2}. For 10 mA cm^{-2}, Q_{gcd} is sustained at 72 mC cm^{-1} (C_A=48 mF cm^{-2}) as shown in Fig. 6(f). The maximum E_A of 33 μWh cm^{-2} is estimated at 1 mA cm^{-2}, and the maximum P_A of 6019 μW cm^{-2} is estimated at 10 mA cm^{-2}, which is higher than that previously reported [53–57] as shown in Fig. 6(g). The stability of AC@NF//NCS@NF was tested by continuous GCD cycling at $j = 6$ mA cm^{-2}. After 10,000 cycles, 89% of the initial Q_{gcd} is retained (Fig. 6h). The inset of Fig. 6h shows the initial and final three consecutive GCD cycles. The shape of the cycles is sustained after 10,000 cycles.

4. Conclusion

The binder-free synthesis of Ni-Co-S nanoflakes on NF was achieved by RPP-ED method. Different NCS@NF electrodes were prepared by repeating RPP-ED cycles for 100, 200, 300, and 400 cycles. Uniform mesoporous interconnected nanoflakes prepared at 300 RPP-ED cycles exhibited a maximum areal capacity of 0.590 C cm^{-2} (590 C g^{-1}) in 2 M KOH. Further increasing the areal capacity up to 2.56 C cm^{-2} (2560 C g^{-1}) was achieved by the addition of 0.1 M of $K_4(CN)_6$. A remarkable stability of 80% over 10,000 GCD cycles shows the advantage of RPP-ED for the binder-free synthesis of NCS@NF caused by improved ionic diffusion at interconnected nanoflakes. Furthermore, the aqueous hybrid SC (AC@NF//NCS@NF) showed an improved charge–discharge potential of 1.5 V with a maximum areal capacity of 165 mC cm^{-1} (C_A = 110 mF cm^{-2}) and maximum areal energy and power density of 33 μWh cm^{-2} and 6019 μW cm^{-2}, respectively, making it suitable for hybrid SC application.

CRediT authorship contribution statement

N. C. Maile: Conceptualization, Experiments & Analysis, Writing – original draft. **S. K. Shinde, D.–Y. Kim, and K. C. Devarayapalli**:

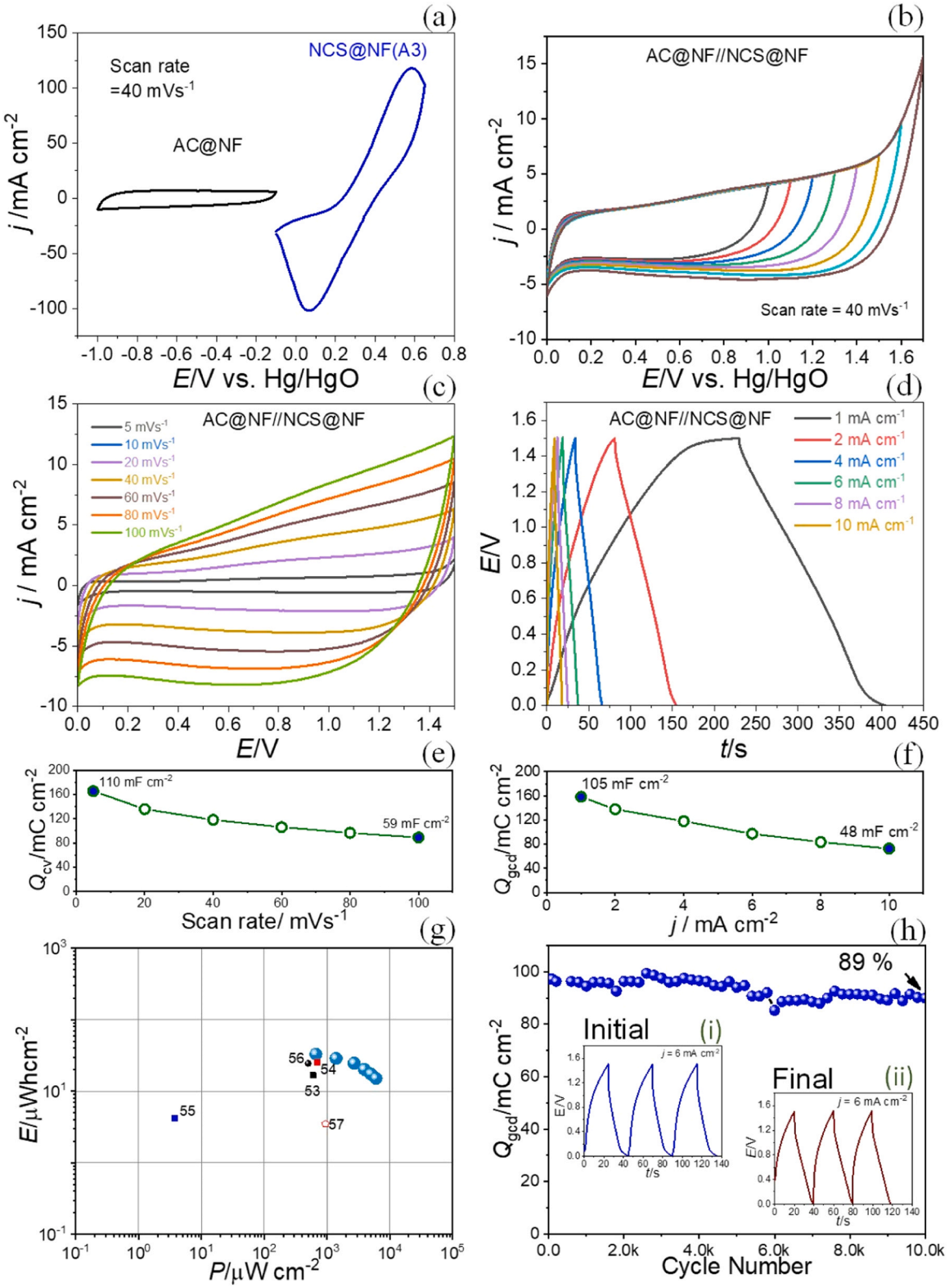

Fig. 6. (a) CV curve of AC@NF and A3 in 2 M KOH + 0.1 M $K_4[Fe(CN)_6]$ at 40 mV s^{-1}, (b) CV curves of AC@NF//NCS@NF at 40 mV s^{-1} for different potential windows, (c) CV curve of SC at different υ values in 2 M KOH + 0.1 M $K_4[Fe(CN)_6]$, (d) GCD curves of SC at different j values in 2 M KOH + 0.1 M $K_4[Fe(CN)_6]$, (e) Plot of the estimated Q_{cv} at different υ values, (f) Plot of the estimated Q_{gcd} at different j values, (g) Ragone plot of AC@NF//NCS@NF, and (h) Plot of the Q_{gcd} at $j = 6$ mA cm^{-2} for 10,000 successive cycles (inset: initial [i] and final [ii] three consecutive GCD cycles).

Experiments & Analysis, Data curation. **Dae Sung Lee**: Conceptualization, Supervision, Resources, Funding acquisition, Project administration, Writing – review & editing.

Declaration of Competing Interest

The authors declare that they have no known competing financial interests or personal relationships that could have appeared to influence the work reported in this paper.

Data Availability

Data will be made available on request.

Acknowledgement

This research was supported by the Basic Science Research Program through the National Research Foundation of Korea (NRF) funded by the Ministry of Education (NRF-2018R1A6A1A03024962) and the Ministry of Science and ICT (NRF-2020R1A2C2100746).

Appendix A. Supporting information

Supplementary data associated with this article can be found in the online version at doi:10.1016/j.jallcom.2023.171845.

References

[1] S. Satpathy, N.K. Misra, D. Kumar Shukla, V. Goyal, B.K. Bhattacharyya, C. S. Yadav, An in-depth study of the electrical characterization of supercapacitors for recent trends in energy storage system, J. Energy Storage 57 (2023), 106198, https://doi.org/10.1016/j.est.2022.106198.

[2] D. Lemian, F. Bode, Battery-supercapacitor energy storage systems for electrical vehicles: a review, Energies 15 (2022) 5683, https://doi.org/10.3390/en15155683.

[3] G.F. Hawes, S. Rehman, Y. Rangom, M.A. Pope, Advanced manufacturing approaches for electrochemical energy storage devices, Int. Mater. Rev. (2022) 1–42, https://doi.org/10.1080/09506608.2022.2086388.

[4] W. Chen, C. Xia, H.N. Alshareef, One-step electrodeposited nickel cobalt sulfide nanosheet arrays for high-performance asymmetric supercapacitors, ACS Nano 8 (2014) 9531–9541, https://doi.org/10.1021/nn503814y.

[5] S.H. Chou, L.Y. Lin, Y.H. Chiu, Pulse reverse electrodeposited nickel cobalt sulfide nanosheets on Ni foam as battery-type electrode for battery supercapacitor hybrids, J. Energy Storage 25 (2019), 100903, https://doi.org/10.1016/j.est.2019.100903.

[6] M. Dong, Z. Chai, J. Li, Z. Wang, One-step potentiostatic electrodeposition of cross-linked bimetallic sulfide nanosheet thin film for supercapacitors, Ionics 26 (2020) 4095–4102, https://doi.org/10.1007/s11581-020-03526-4.

[7] D.Y. Kim, G.S. Ghodake, N.C. Maile, A.A. Kadam, D. Sung Lee, V.J. Fulari, S. K. Shinde, Chemical synthesis of hierarchical $NiCo_2S_4$ nanosheets like nanostructure on flexible foil for a high performance supercapacitor, Sci. Rep. 7 (2017) 1–10, https://doi.org/10.1038/s41598-017-10218-z.

[8] S.K. Shinde, M.B. Jalak, G.S. Ghodake, N.C. Maile, V.S. Kumbhar, D.S. Lee, V. J. Fulari, D.Y. Kim, Chemically synthesized nanoflakes-like $NiCo_2S_4$ electrodes for high-performance supercapacitor application, Appl. Surf. Sci. 466 (2019) 822–829, https://doi.org/10.1016/j.apsusc.2018.10.100.

[9] W. Kong, C. Lu, W. Zhang, J. Pu, Z. Wang, Homogeneous core-shell $NiCo_2S_4$ nanostructures supported on nickel foam for supercapacitors, J. Mater. Chem. A 3 (2015) 12452–12460, https://doi.org/10.1039/c5ta02432c.

[10] Z. Lv, Q. Zhong, Z. Zhao, Y. Bu, Facile synthesis of hierarchical nickel–cobalt sulfide quadrangular microtubes and its application in hybrid supercapacitors, J. Mater. Sci. Mater. Electron. 28 (2017) 18064–18074, https://doi.org/10.1007/s10854-017-7750-4.

[11] J. Li, F. Luo, Q. Zhao, W. Liu, D. Xiao, Low-temperature coprecipitation synthesis of amorphous nickel cobalt sulfide nanoparticles for high-performance supercapacitors, J. Mater. Sci. Mater. Electron. 30 (2019) 14538–14546, https://doi.org/10.1007/s10854-019-01825-9.

[12] Y. Liu, Q. Lu, Z. Huang, S. Sun, B. Yu, U. Evariste, G. Jiang, J. Yao, Electrodeposition of Ni-Co-S nanosheet arrays on N-doped porous carbon nanofibers for flexible asymmetric supercapacitors, J. Alloy. Compd. 762 (2018) 301–311, https://doi.org/10.1016/j.jallcom.2018.05.239.

[13] M. Wang, L. An, M. Wu, S. Zhang, Y. Feng, X. Zhang, J. Mi, Self-template synthesis of nickel cobalt sulfide hollow nanotubes for high-performance battery-type supercapacitors, J. Electrochem. Soc. 168 (2021), 060510, https://doi.org/10.1149/1945-7111/ac0458.

[14] S. Islam, M.M. Mia, S.S. Shah, S. Naher, M.N. Shaikh, M.A. Aziz, A.J.S. Ahammad, 2022. Recent Advancements in Electrochemical Deposition of Metal-Based Electrode Materials for Electrochemical Supercapacitors, 2022. https://doi.org/10.1002/tcr.202200013.

[15] N.C. Maile, M. Moztahida, A.A. Ghani, M. Hussain, K. Tahir, B. Kim, S.K. Shinde, V. J. Fulari, D.S. Lee, Electrochemical synthesis of binder-free interconnected nanosheets of Mn-doped Co_3O_4 on Ni foam for high-performance electrochemical energy storage application, Chem. Eng. J. 421 (2021), 129767, https://doi.org/10.1016/j.cej.2021.129767.

[16] K.S. Anuratha, S. Mohan, S.K. Panda, Pulse reverse electrodeposited $NiCo_2S_4$ nanostructures as efficient counter electrodes for dye-sensitized solar cells, N. J. Chem. 40 (2016) 1785–1791, https://doi.org/10.1039/c5nj02565f.

[17] P.S. Shinde, A. Annamalai, J.Y. Kim, S.H. Choi, J.S. Lee, J.S. Jang, Fine-tuning pulse reverse electrodeposition for enhanced photoelectrochemical water oxidation performance of α-Fe_2O_3 photoanodes, J. Phys. Chem. C. 119 (2015) 5281–5292, https://doi.org/10.1021/jp5100186.

[18] C.C. Hu, K.H. Chang, Y.T. Wu, C.Y. Hung, C.C. Lin, Y.T. Tsai, Pulse deposition of large area, patterned manganese oxide nanowires in variable aspect ratios without templates, Electrochem. Commun. 10 (2008) 1792–1796, https://doi.org/10.1016/j.elecom.2008.09.011.

[19] B.K. Kim, M.J. Kim, J.J. Kim, Modulating the active sites of nickel phosphorous by pulse-reverse electrodeposition for improving electrochemical water splitting, Appl. Catal. B Environ. 308 (2022), 121226, https://doi.org/10.1016/j.apcatb.2022.121226.

[20] L. Wan, C. He, D. Chen, J. Liu, Y. Zhang, C. Du, M. Xie, J. Chen, In situ grown NiFeP@$NiCo_2S_4$ nanosheet arrays on carbon cloth for asymmetric supercapacitors, Chem. Eng. J. 399 (2020), 125778, https://doi.org/10.1016/j.cej.2020.125778.

[21] P. Dhaiveegan, Y.K. Hsu, Y.H. Tsai, C.K. Hsieh, J.Y. Lin, Pulse-reversal deposition of Ni_3S_2 thin films on carbon fiber cloths for supercapacitors, Surf. Coat. Technol. 350 (2018) 1003–1009, https://doi.org/10.1016/j.surfcoat.2018.02.079.

[22] S. Arunpandiyan, G. Hariharan, A. Raja, R. Packiaraj, S. Bharathi, A. Arivarasan, Significance of redox additive electrolyte over energy and power densities of mixed metal vanadate-based supercapattery device, ACS Appl. Electron. Mater. 4 (2022) 5884–5892, https://doi.org/10.1021/acsaelm.2c01049.

[23] S. Arunpandiyan, S. Bharathi, A. Pandikumar, S. Ezhil Arasi, A. Arivarasan, Structural analysis and redox additive electrolyte based supercapacitor performance of ZnO/CeO_2 nanocomposite, Mater. Sci. Semicond. Process. 106 (2020), 104765, https://doi.org/10.1016/j.mssp.2019.104765.

[24] N. Maile, S. Shinde, Y. Lim, B. Kim, A.A. Ghani, K. Tahir, M. Hussain, J. Jang, D. S. Lee, Enhanced electrochemical performance of hybrid composite microstructure of $CuCo_2O_4$ microflowers-NiO nanosheets on 3D Ni foam as positive electrode for stable hybrid supercapacitors, Ceram. Int. 49 (2023) 1800–1810, https://doi.org/10.1016/j.ceramint.2022.09.143.

[25] K.J. Babu, R.T. Kumar, D.J. Yoo, S.M. Phang, G. Kumar, Electrodeposited nickel cobalt sulfide flowerlike architectures on disposable cellulose filter paper for enzyme-free glucose sensor applications, ACS Sustain. Chem. Eng. 6 (2018) 16982–16989, https://doi.org/10.1021/acssuschemeng.8b04340.

[26] A.V. Munde, B.B. Mulik, R.P. Dighole, S.C. Dhawale, L.S. Sable, A.T. Avhale, B. R. Sathe, Bi_2O_3@Bi nanoparticles for ultrasensitive electrochemical determination of thiourea: monitoring towards environmental pollutants, Electrochim. Acta 394 (2021), 139111, https://doi.org/10.1016/j.electacta.2021.139111.

[27] E. Chassaing, M.P. Roumegas, M.F. Trichet, Electrodeposition of Ni-Mo alloys with pulse reverse potentials, J. Appl. Electrochem. 25 (1995) 667–670, https://doi.org/10.1007/BF00241928.

[28] F. Wang, Y. Wu, K. Lu, L. Gao, B. Ye, A simple, rapid and green method based on pulsed potentiostatic electrodeposition of reduced graphene oxide on glass carbon electrode for sensitive voltammetric detection of sophoridine, Electrochim. Acta 141 (2014) 82–88, https://doi.org/10.1016/j.electacta.2014.07.018.

[29] R. Zou, Y. Wang, M. Hu, Y. Wei, T. Fujita, Analysis of ruthenium electrodeposition in the nitric acid medium, J. Phys. Chem. C. 126 (2022) 4329–4337, https://doi.org/10.1021/acs.jpcc.1c09371.

[30] I.-H. Lo, J.-Y. Wang, K.-Y. Huang, J.-H. Huang, W.P. Kang, Synthesis of $Ni(OH)_2$ nanoflakes on ZnO nanowires by pulse electrodeposition for high-performance supercapacitors, J. Power Sources 308 (2016) 29–36, https://doi.org/10.1016/j.jpowsour.2016.01.041.

[31] P.K. Kannan, C. Hu, H. Morgan, C.S. Rout, One-step electrodeposition of $NiCo_2S_4$ nanosheets on patterned platinum electrodes for non-enzymatic glucose sensing, Chem. - Asian J. 11 (2016) 1837–1841, https://doi.org/10.1002/asia.201600362.

[32] H.-L. Chen, P.-S. Wu, J.-J. Wu, Binder-free metal sulfide composite nanosheet array electrodes for Li-Ion batteries, ACS Sustain. Chem. Eng. 7 (2019) 17100–17106, https://doi.org/10.1021/acssuschemeng.9b03329.

[33] C. Xia, P. Li, A.N. Gandi, U. Schwingenschlögl, H.N. Alshareef, Is $NiCo_2S_4$ Really a Semiconductor? Chem. Mater. 27 (2015) 6482–6485, https://doi.org/10.1021/acs.chemmater.5b01843.

[34] X. Wang, S.-X. Zhao, L. Dong, Q.-L. Lu, J. Zhu, C.-W. Nan, One-step synthesis of surface-enriched nickel cobalt sulfide nanoparticles on graphene for high-performance supercapacitors, Energy Storage Mater. 6 (2017) 180–187, https://doi.org/10.1016/j.ensm.2016.11.005.

[35] Y. Chen, L. Wang, H. Gan, Y. Jiang, J. Feng, J. Liu, X. Shi, Designing NiS/CoS decorated $NiCo_2S_4$ nanoflakes towards high performance binder-free supercapacitors, J. Energy Storage 47 (2022), 103625, https://doi.org/10.1016/j.est.2021.103625.

[36] J. Xiao, X. Zeng, W. Chen, F. Xiao, S. Wang, High electrocatalytic activity of self-standing hollow $NiCo_2S_4$ single crystalline nanorod arrays towards sulfide redox shuttles in quantum dot-sensitized solar cells, Chem. Commun. 49 (2013) 11734, https://doi.org/10.1039/c3cc44242j.

[37] J. Gong, W. Luo, Y. Zhao, M. Xie, J. Wang, J. Yang, Y. Dai, Co_9S_8/$NiCo_2S_4$ core-shell array structure cathode hybridized with PPy/MnO_2 core-shell structure anode

for high-performance flexible quasi-solid-state alkaline aqueous batteries, Chem. Eng. J. 434 (2022), 134640, https://doi.org/10.1016/j.cej.2022.134640.
[38] N.C. Maile, A.A. Ghani, S.K. Shinde, B. Kim, Y. Lim, K. Tahir, K.C. Devarayapalli, S. V. Mohite, J. Jang, D.S. Lee, Electrochemical studies of $Ni(OH)_2$, NiO, and Ni_3S_2 nanostructures on Ni-foam toward binder-free positive electrode for hybrid supercapacitor application, Int. J. Energy Res. 46 (2022) 22501–22515, https://doi.org/10.1002/er.8553.
[39] R. Ding, M. Zhang, Y. Yao, H. Gao, Crystalline $NiCo_2S_4$ nanotube array coated with amorphous NiCoxSy for supercapacitor electrodes, J. Colloid Interface Sci. 467 (2016) 140–147, https://doi.org/10.1016/j.jcis.2015.12.057.
[40] J. Gong, W. Luo, Y. Zhao, J. Wang, S. Wang, C. Hu, J. Yang, Y. Dai, Surface engineering of Ni wires and rapid growth strategy of Ni-MOF synergistically contribute to high-performance fiber-shaped aqueous battery, Small 18 (2022), 2204346, https://doi.org/10.1002/smll.202204346.
[41] G.S. Kaliaraj, A. Ramadoss, Nickel–zinc sulfide nanocomposite thin film as an efficient cathode material for high-performance hybrid supercapacitors, Mater. Sci. Semicond. Process. 105 (2020), 104709, https://doi.org/10.1016/j.mssp.2019.104709.
[42] Q. Hu, X. Zou, Y. Huang, Y. Wei, Ya Wang, F. Chen, B. Xiang, Q. Wu, W. Li, Graphene oxide-drove transformation of NiS/Ni_3S_4 microbars towards Ni3S4 polyhedrons for supercapacitor, J. Colloid Interface Sci. 559 (2020) 115–123, https://doi.org/10.1016/j.jcis.2019.10.010.
[43] Z. Li, S. He, C. Ji, H. Mi, C. Lei, Z. Li, H. Pang, Z. Fan, C. Yu, J. Qiu, Hierarchical bimetallic hydroxides built by porous nanowire-lapped bundles with ultrahigh areal capacity for stable hybrid solid-state supercapacitors, Adv. Mater. Interfaces 6 (2019), 1900959, https://doi.org/10.1002/admi.201900959.
[44] J.S. Sanchez, A. Pendashteh, J. Palma, M. Anderson, R. Marcilla, Insights into charge storage and electroactivation of mixed metal sulfides in alkaline media: NiCoMn ternary metal sulfide nano-needles forming core–shell structures for hybrid energy storage, J. Mater. Chem. A. 7 (2019) 20414–20424, https://doi.org/10.1039/C9TA04322E.
[45] A.R. Nath, N. Sandhyarani, SILAR deposited nickel sulphide-nickel hydroxide nanocomposite for high performance asymmetric supercapacitor, Electrochim. Acta 356 (2020), 136844, https://doi.org/10.1016/j.electacta.2020.136844.
[46] M. Shahi, F. Hekmat, S. Shahrokhian, Hybrid supercapacitors constructed from double-shelled cobalt-zinc sulfide/copper oxide nanoarrays and ferrous sulfide/graphene oxide nanostructures, J. Colloid Interface Sci. 585 (2021) 750–763, https://doi.org/10.1016/j.jcis.2020.10.055.
[47] M.Z. Iqbal, J. Khan, A.M. Afzal, S. Aftab, Exploring the synergetic electrochemical performance of cobalt sulfide/cobalt phosphate composites for supercapattery devices with high-energy and rate capability, Electrochim. Acta 384 (2021), 138358, https://doi.org/10.1016/j.electacta.2021.138358.
[48] J. Yu, X. Pang, Q. Yin, D. Chen, H. Dong, Q. Zhang, J. Sui, L. Sui, L. Dong, Metal-organic frameworks supported Ni–Co–S nanosheet arrays for advanced hybrid supercapacitors, Int. J. Hydrog. Energy 47 (2022) 39265–39275, https://doi.org/10.1016/j.ijhydene.2022.09.065.
[49] A.I. Abdel-Salam, S.Y. Attia, F.I. El-Hosiny, M.A. Sadek, S.G. Mohamed, M. M. Rashad, Facile one-step hydrothermal method for $NiCo_2S_4$/rGO nanocomposite synthesis for efficient hybrid supercapacitor electrodes, Mater. Chem. Phys. 277 (2022), 125554, https://doi.org/10.1016/j.matchemphys.2021.125554.
[50] N. Maile, S.K. Shinde, A.V. Fulari, D.S. Lee, V.J. Fulari, Galvanostatic synthesis of $MnCo_2O_4$ nanoflakes like thin films: effect of deposition parameter on supercapacitive performance, Ion. (Kiel.) 27 (2021) 1677–1688, https://doi.org/10.1007/s11581-021-03909-1.
[51] G. Zeng, Y. Chen, L. Chen, P. Xiong, M. Wei, Hierarchical cerium oxide derived from metal-organic frameworks for high performance supercapacitor electrodes, Electrochim. Acta 222 (2016) 773–780, https://doi.org/10.1016/j.electacta.2016.11.035.
[52] D. Jain, J. Kanungo, S.K. Tripathi, Synergistic approach with redox additive for the development of environment benign hybrid supercapacitor, J. Electrochem. Soc. 166 (2019) A3168–A3181, https://doi.org/10.1149/2.0321914jes.
[53] X. Chu, Y. Wang, L. Cai, H. Huang, Z. Xu, Y. Xie, C. Yan, Q. Wang, H. Zhang, H. Li, W. Yang, Boosting the energy density of aqueous MXene-based supercapacitor by integrating 3D conducting polymer hydrogel cathode, SusMat 2 (2022) 379–390, https://doi.org/10.1002/sus2.61.
[54] C. Shi, J. Sun, Y. Pang, Y.P. Liu, B. Huang, B.T. Liu, A new potassium dual-ion hybrid supercapacitor based on battery-type $Ni(OH)_2$ nanotube arrays and pseudocapacitor-type V_2O_5-anchored carbon nanotubes electrodes, J. Colloid Interface Sci. 607 (2022) 462–469, https://doi.org/10.1016/j.jcis.2021.09.011.
[55] C.C.H. Tran, J. Santos-Peña, C. Damas, Electrodeposited manganese oxide supercapacitor microelectrodes with enhanced performance in neutral aqueous electrolyte, Electrochim. Acta 335 (2020), 135564, https://doi.org/10.1016/j.electacta.2019.135564.
[56] S.S. Shah, M.A. Alfasane, I.A. Bakare, M.A. Aziz, Z.H. Yamani, Polyaniline and heteroatoms–enriched carbon derived from Pithophora polymorpha composite for high performance supercapacitor, J. Energy Storage 30 (2020), 101562, https://doi.org/10.1016/j.est.2020.101562.
[57] C. Wang, Y. Zhan, L. Wu, Y. Li, J. Liu, High-voltage and high-rate symmetric supercapacitor based on MnO_2-polypyrrole hybrid nanofilm, Nanotechnology 25 (2014), https://doi.org/10.1088/0957-4484/25/30/305401.